

Musah, J.-D., Linlin, L., Guo, C., Novitskii, A., Ilyas, A. O., Serhiiienko, I., Khovaylo, V., Roy, V. A.L. and Lawrence Wu, C.-M. (2022) Enhanced thermoelectric performance of bulk bismuth selenide: synergistic effect of indium and antimony co-doping. *ACS Sustainable Chemistry and Engineering*, 10(12), pp. 3862-3871.
(doi: [10.1021/acssuschemeng.1c07256](https://doi.org/10.1021/acssuschemeng.1c07256))

There may be differences between this version and the published version.
You are advised to consult the published version if you wish to cite from it.

<http://eprints.gla.ac.uk/267875/>

Deposited on 7 April 2022

Enlighten – Research publications by members of the University of Glasgow
<http://eprints.gla.ac.uk>

Enhanced Thermoelectric Performance of Bulk Bismuth Selenide: Synergistic Effect of Indium and Antimony co-doping

Jamal-Deen Musah[†], Liu Linlin[†], Chen Guo[†], Andrei Novitskii[‡], AbdulMojeed O. Ilyas^{††}, Illia Serhiienko[‡], Vladimir Khovaylo[‡], Vellaisamy A. L. Roy^{‡‡*}, Chi-Man Lawrence Wu^{†*}

Affiliation:

[†]Department of Materials Science and Engineering, City University of Hong Kong, Kowloon, Hong Kong, S.A.R.

[‡]Academic Center for Energy Efficiency, National University of Science and Technology "MISiS", Leninsky ave. 4, Moscow 119049, Russia

^{††}Department of Physics, City University of Hong Kong, Kowloon, Hong Kong, S.A.R

^{‡‡}James Watt School of Engineering, University of Glasgow, Glasgow G128QQ, UK

**Corresponding authors:*

Roy.Vellaisamy@glasgow.ac.uk

lawrence.wu@cityu.edu.hk

Abstract

The thermoelectric performance of pristine Bi₂Se₃ is inferior to that of Bi₂Te₃. Therefore, the study on Bi₂Se₃ has faced a decline. The lower performance is due to the low power factor and high thermal conductivity. In recent years, single aliovalent doping has been adopted to improve the thermoelectric performance of Bi₂Se₃. Here, we adopt an isovalent co-doping approach using indium and antimony to create a manifold enhancement in the thermoelectric performance of Bi₂Se₃ via the creation of neutral impurities and deep defect states. A high figure of merit ($ZT = 0.47$) is obtained at 473K for a doping concentration of 0.1 at.%. The thermoelectric performance obtained for the Bi_{2-x}In_xSb_{2x/3}Se₃, $x = 0.1$ at.% is comparable to several reports for pristine Bi₂Te₃. Our DFT

calculation reveals an underlying deep defect state located at ~15 eV below the Fermi level. This leads to enhanced electronic properties via density of state optimization induced by the co-doping. The isovalent doping is expected to create neutral impurities, which causes less scattering to conduction electrons while absorbing phonon vibration, thus improving the thermoelectric performance.

KEYWORDS; Thermoelectric (TE) Enhancement, Metal Chalcogenides, Power Factor (PF), Bismuth Selenide, Co-doping, Isovalent doping

Introduction

Commercialized thermoelectric materials used for harvesting waste heat energy from the bismuth chalcogenide (Bi-Chs) family are mainly doped Bi_2Te_3 materials. Bi_2Te_3 materials are known for their high power factor (PF), which is the product of electrical conductivity and Seebeck coefficient, and considerably low thermal conductivity. Although Bi_2Se_3 belongs to the bismuth chalcogenides group, it is less regarded for device fabrication due to its poor thermoelectric performance. Enhancing the TE properties of Bi-Chs remains a significant challenge for researchers due to the conflicting dependency of the TE transport properties (Seebeck coefficient, S , electrical conductivity, σ and the total thermal conductivity, κ_T) that define the efficiency of the TE device. Bi_2Se_3 possesses a rhombohedral layered structure stacked along the c -axis with van der Waals gaps that allow doping. The voids allow for dopant intercalation, which arrests phonon vibration and decreases the total thermal conductivity. Due to this, several single and multiple dopants have been utilized in bismuth chalcogenides to further improve their electronic properties. The dimensionless figure of merit (ZT) of any TE material is determined by the relation $ZT = \frac{\sigma S^2}{\kappa_T} T$.¹ From this relation, it is evident that materials with high electrical conductivity and Seebeck coefficient and or considerably low κ_T are of desired interest. Several reported studies focus on band engineering,²⁻⁴ point defect,⁵ nanostructuring,⁶ doping⁷⁻⁹ to improve the PF of TE materials.¹⁰ Controlled doping has shown usefulness in enhancing the TE performance of Bi_2Te_3 -based materials.¹¹

The past few decades earmarked the first generation of bulk thermoelectric materials. These materials exhibited an efficiency of about 5 - 6% and a thermoelectric figure of merit of about 0.8 – 1.0.¹² Most of these materials, which saw the light of the day for practical usage, fall under the metal chalcogenides class. The most recognised state of art TE material for room temperature application is Bi₂Te₃.¹³ Researchers have published several strategies to improve TE performance, including band engineering of thermoelectric materials,² synthesis of chalcogenides,¹⁴ wearable thermoelectric power generation,¹⁵ nanostructured thermoelectric materials.^{16,17} Bi₂Te₃/Sb₂Te₃-based materials are the best TE materials for near room-temperature applications, with ZT values ranging between 1 and 2.¹⁸ Thermoelectric devices have numerous applications, including real-time monitoring of personal health (electrocardiographic),^{19–21} polymer electrolyte membrane fuel cell,²² and heat pump,²³ where the body heat is harvested and used by a wearable device for monitoring the health of human. Despite the high TE performance of Bi₂Te₃-based materials, the scarcity and toxicity of telluride make it crucial to devise any means possible to improve cheaper and less toxic Bi₂Se₃-based material alternatives significantly. After Sun *et al.*²⁴ published their studies on Cu-doped Cu_xBi₂Se₃ with a maximum ZT of 0.54 at 590 K in 2015, no other work has shown such a high ZT for Bi₂Se₃ thermoelectric material. The high ZT for Cu_{0.01}Bi₂Se₃ can be attributed to the enhanced thermal conductivity reduction caused by the increased phonon scattering.

Herein, we show that indium (In) and antimony (Sb) co-doping in Bi₂Se₃ rhombohedral structure is a practical approach in promoting simultaneous enhancement in Seebeck coefficient and electrical conductivity as well as a drastic means to reduce the thermal conductivity. The co-doped Bi₂Se₃ samples (Bi_{2-x}In_xSb_{2x/3}Se₃) is synthesized through a single step thermal route followed by appropriate characterization methods. The In substitution at Bi site will modify the band structure to enhance the Seebeck coefficient and electrical conductivity. Simultaneously, the insertion of an antimony atom in Bi₂Se₃ is expected to arrest phonon vibration and reduce the lattice thermal conductivity. Again, the choice of In atom as a substitute for Bi atom is due to their similar electronic structures and the tendency to promote neutral ions that control the overall scattering of conduction electrons. Due to the smaller atomic size of Sb (133 pm), it is suitable as an intercalant in the Bi₂Se₃

layers. The presence of Sb atoms within the van der Waals gaps of the In doped bismuth selenide materials causes rattling, which reduces thermal conductivity.

Experimental Section

Synthesis of $\text{Bi}_{2-x}\text{In}_x\text{Sb}_{2x/3}\text{Se}_3$ nanostructures ($x = 0, 0.05, 0.1, 0.2$)

Selenium powder (Se powder, J&K Scientific Ltd, 99%), Bismuth (Bi) nitrate pentahydrate ($\text{Bi}(\text{NO}_3)_3 \cdot 5\text{H}_2\text{O}$, J&K Scientific Ltd, 99 %), Antimony chloride (SbCl_3 - Aldrich, 99.99%), Indium chloride (InCl_3 - Aldrich, 99.99%), 2-methoxy ethanol anhydrous (Sigma Aldrich, 99.8%) and ethanolamine (ACS reagent, Aldrich $\geq 99.0\%$) were used without any further purification. The synthesis of $\text{Bi}_{2-x}\text{In}_x\text{Sb}_{2x/3}\text{Se}_3$ was carried out similar to the procedure already reported.²⁵ In a typical synthesis method, a mixture of 2-methoxy ethanol and ethanolamide was preheated at 373K for 30 minutes. Then 1 mmol of bismuth nitrate and 1.5 mmol of Se powder were added to the above mixture and then subjected to continual stirring for 3 hours on a hot plate kept at 473K. Lastly, the hot plate was turned off, and the precipitate was collected through centrifugation, followed by washing multiple times with water and ethanol. The final powder was then dried at 343K in an open oven for 6 hours. It is important to mention that, for ease in referencing, all our synthesized In and Sb co-doped $\text{Bi}_{2-x}\text{In}_x\text{Sb}_{2x/3}\text{Se}_3$ samples are hereafter abbreviated as BS ($x = 0$ at.%), BISS-0.05 ($x = 0.05$ at.%), BISS-0.1 ($x = 0.1$ at.%) and BISS-0.2 ($x = 0.2$ at.%). The densities of the prepared samples, 6.71 gcm^{-3} , 6.58 gcm^{-3} , 6.45 gcm^{-3} and 6.24 gcm^{-3} for BS, BISS-0.05, BISS-0.1 and BISS-0.2, respectively, are in good agreement with those in the literature.⁸

Characterization of $\text{Bi}_{2-x}\text{In}_x\text{Sb}_{2x/3}\text{Se}_3$ nanostructures

The measurement of electrical conductivity (σ), Seebeck coefficient (S), and thermal conductivity (k_T) of all the $\text{Bi}_{2-x}\text{In}_x\text{Sb}_{2x/3}\text{Se}_3$ samples were obtained from room temperature to 473 K. The 13 mm disc-shaped samples were formed into a rectangular bar ($12.7 \text{ mm} \times 7 \text{ mm} \times 0.5 \text{ mm}$) for the σ and S measurement. Then the laser flash method (NETZSCH, LFA457), the scanning calorimetry (NETZSCH, DSC 404F) and Archimedes principle were used for the measurement of the thermal

diffusivity (λ), heat capacity (C_p) and density (ρ), respectively. With the C_p , ρ and λ known, the total thermal conductivity (K_T) is calculated from the relation; $K_T = \rho \times \lambda \times C_p$. It is worth mentioning that the σ and S were measured within an error of 8% while that of the thermal conductivity is 9%. More so, using a commercial Hall-effect system (ECOPIA HMS-5300) in the *van der Pauw* configuration, the Hall coefficient, R_H was measured at 300K under a magnetic field of 0.5T and a current of 20 mA. Then the Hall carrier mobility, μ_H and carrier density, n_H were calculated according to $\mu_H = \sigma R_H$ and $n_H = \frac{1}{eR_H}$, respectively. The errors in the Hall coefficient and Hall mobility measurements were less than 5%. Thus, the overall uncertainty for all measurements involving the ZT calculation was less than 20%.

Computational details

The density functional theory (DFT) calculations were applied to obtain an insight into the In and Sb co-doped Bi_2Se_3 electronic band structure. The DMol³ program using the Perdew–Burke–Ernzerhof (PBE) of generalized-gradient approximation (GGA) function²⁶ was adopted in a typical calculation method. Again, the plane wave kinetic energy cutoff was set at 500 eV. The co-doped $\text{Bi}_{2-x}\text{In}_x\text{Sb}_{2x/3}\text{Se}_3$ materials were modelled using the $2 \times 2 \times 1$ supercell. The DN basic set described the whole system with polarization function (DNP). Again, the DFT Semi-core Pseudopotentials (DSPP) core treatment was taken to replace the core electrons with a single effective potential.²⁷ More importantly, the k-point of the Brillion zone was maintained as $3 \times 3 \times 1$ for the geometry optimization and $6 \times 6 \times 3$ for high-quality electronic structure calculation.

Results and Discussion

Structural properties of the $\text{Bi}_{2-x}\text{In}_x\text{Sb}_{2x/3}\text{Se}_3$ nanostructures

To characterize the formation of the $\text{Bi}_{2-x}\text{In}_x\text{Sb}_{2x/3}\text{Se}_3$ structure, the X-ray diffraction technique is used to determine the final black products' crystal phase, as shown in Figure 1. It is observed that the crystal structure of the Bi_2Se_3 shows no deviation upon the introduction of the co-dopants. This is

depicted in Figure 1a, where there is an absence of a new phase in the doped samples. It is thus important to mention that despite the presence of the dopants of different ionic sizes ($\text{In}^{3+} \rightarrow 0.8 \text{ \AA}$, $\text{Sb}^{3+} \rightarrow 0.76 \text{ \AA}$) compared to the host ($\text{Bi}^{3+} \rightarrow 1.03 \text{ \AA}$), the XRD patterns of the co-doped samples show a single phase composition and hence the result is highly consistent with that of hexagonal JCDPS # 33-0214 for pristine Bi_2Se_3 . However, we observed a noticeable lattice shift to a lower 2θ (Figure 1b) for the highly doped sample ($x = 0.2 \text{ at.}\%$). This implies the impurity atoms substitute the host (In) or occupy the interstitial sites (Sb) without much lattice interference for the less doped samples ($x < 0.2 \text{ at.}\%$). As the doping amount reaches $x = 0.2 \text{ at.}\%$, more Bi atoms are replaced by In as Sb intercalate the Bi_2Se_3 network, leading to high lattice expansion in the in-plane axis,²⁸ which is evident in Figure 1b and Table S1.

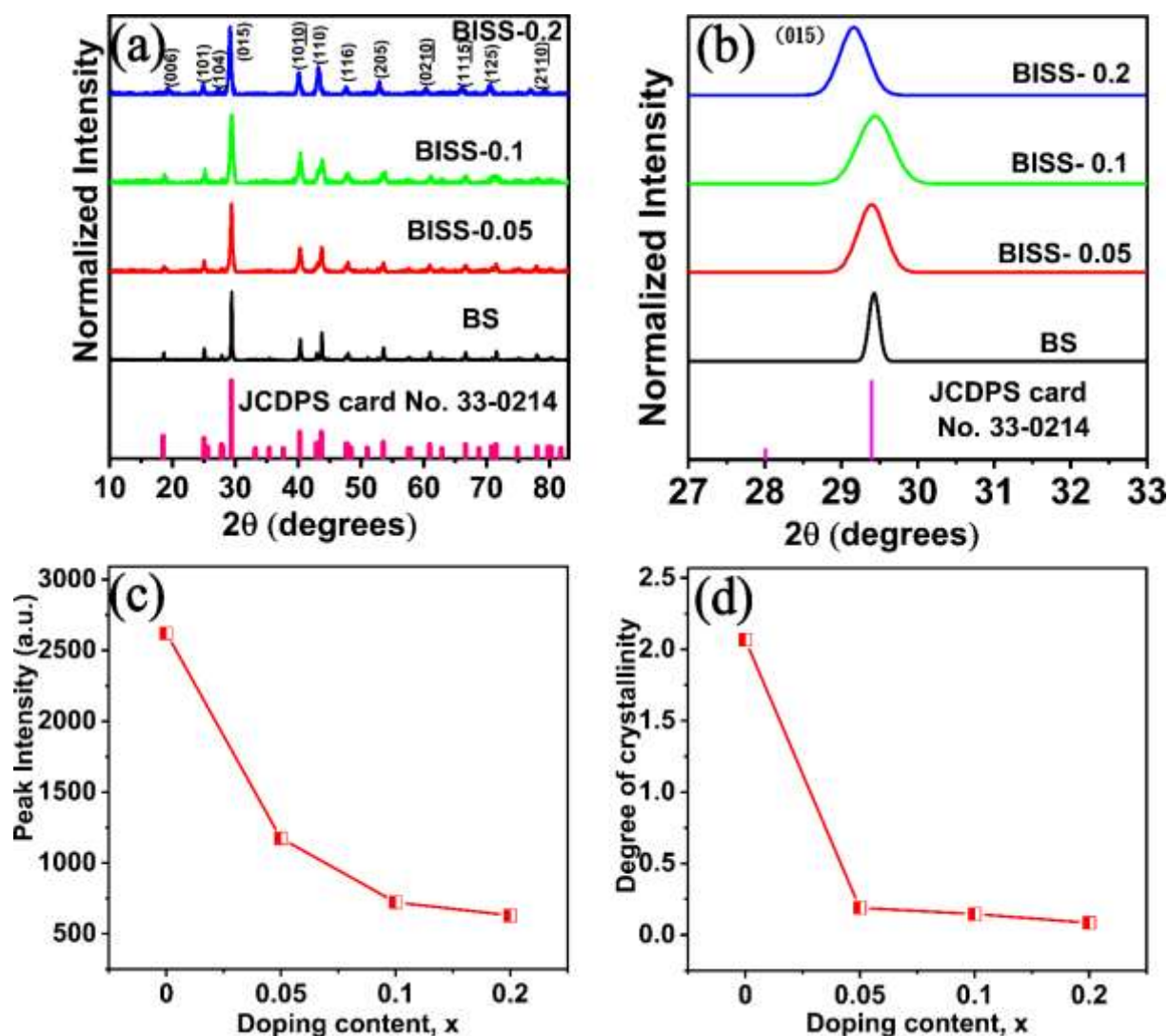


Figure 1. (a) the normalized XRD pattern (b) shift in the (015) plane (c) peak intensity of the (015) plane dependence on the doping content (d) the degree of crystallinity dependence on the doping content of all the synthesized BISS samples

We also note that the diffraction peaks of all the co-doped samples show broadened peaks (larger full Width half maximum, FWHM), which is caused by the lattice strain and crystallite size. The increase in FWHM with doping suggest that the crystallite sizes of all the BISS samples are smaller than that of the pristine. Accordingly, the calculated (using Eqn S1 and Eqn S2) lattice parameter ($a = b$) of the hexagonal phase of Bi_2Se_3 is found to increase with doping concentration, which explains the in-plane crystal lattice expansion while that of the vertical plane (out-of-plane) diminishes upon doping. As the lattice parameters of the impurity (In_2Se_3 ; $a = b = 7.1286 \text{ \AA}$ and $c = 19.3820 \text{ \AA}$)²⁹ are different from that of the host, Bi_2Se_3 ($a = b = 4.13 \text{ \AA}$, $c = 28.58 \text{ \AA}$),³⁰ it is expected that as more In atoms substitute the Bi ones, the significant difference between the in-plane and out-of-plane lattice parameters creates in-plane lattice expansion and out-of-plane contraction in the final bulk structure. Therefore, variable lattice distortion (contraction and expansion) coexisting in the co-doped Bi_2Se_3 structure is not uncommon.³¹ Elsewhere, Samoilov et al.³¹ have shown that doping of indium in lead telluride (PbTe) causes lattice parameter decrease for doping content (x) less than 0.6 at.%. However, as the In concentration increases ($x > 0.6$ at.%), a noticeable rise in the lattice parameter is observed. This, thus, results in a lattice volume decrease. It is worth pointing out that the expansion found in the in-plane axis could not compensate for much contraction in the out-of-plane, as shown in Table S1. The in-plane lattice parameter increases with co-doping while the out-of-plane lattice decreases for the entire doping range. Again, the peak intensity (Figure 1c) of the highly intense peak (015) and the degree of crystallinity (using Eqn S3, Supporting Information) of all the samples decreases with doping until $x = 0.2$ at.%. The peak intensity trend corresponded well with the degree of crystallinity (Figure 1d) of all the samples. Using the data obtained from the XRD characterization, the average crystallite size (using Eqn S4) and the microstrain (Eqn S5) in all the studied samples were estimated using the same procedure reported in our previous studies.³⁰ The obtained crystallite size and

microstrain (Figure S1a) shows an inverse relationship consistent with literature,³² and correspondingly, the XRD relative intensity of the (015), (1010) and (205) are chosen and compared in Figure S1b. The variation in the respective intensity and the corresponding low 2θ shift (expansion) is shown. The crystallite sizes reduce drastically from 420 nm (pristine) to 145 nm ($x = 0.2$ at.%). The decreased crystallite size is significant for forming numerous grain boundaries, which hinders the propagation of phonon transport and hence causes a reduction in thermal conductivity. Accordingly, the microstrain is calculated from Eqn S5. The co-doping yielded an increase in microstrain with doping from the pristine (0.9×10^{-3}) to the highly doped sample (2.4×10^{-3}). Installing impurity atoms into the interstitial gaps in a crystal structure and substituting a host atom with a foreign atom with a different atomic size is expected to cause straining of the crystal lattice³³ due to the distribution of the lattice parameters arising from the crystal imperfections induced by the dopants.

Numerically, we estimate the impact of co-doping on the lattice of the pristine bismuth selenide material. First, the doping-induced crystal lattice dislocation (using Eqn S6) is obtained (Table S2) using the procedure already reported elsewhere.²⁵ It was found that, with increasing doping, the lattice dislocation increased from $0.71 \times 10^{15} \text{ m}^{-2}$ for the pristine to $5.97 \times 10^{15} \text{ m}^{-2}$ for BISS-0.2. The increase in dislocation density with doping is due to the increase in the concentration of the dopants (with varying atomic sizes) in the host crystal lattice breaking the regular atomic order.

The presence of dislocation defects in materials leads to phonon-dislocation scattering, which results in a colossal reduction in lattice thermal conductivity and hence total thermal conductivity.³⁴ Low K_T materials promote high TE performance since the thermoelectric figure of merit is inversely proportional to the total thermal conductivity.

More so, the effect of co-doping on the chemical structure of the final $\text{Bi}_{2-x}\text{In}_x\text{Sb}_{2x/3}\text{Se}_3$ samples were examined using Raman spectroscopy (Figure 2). The two prominent peaks located at 129.3 cm^{-1} and 172.6 cm^{-1} were assigned to the E_g^2 and A_{1g}^2 vibrational modes, respectively (Figure 2a). A peak shift (Figure 2b) is noticed for all the BISS samples. This indicates that the doped Bi_2Se_3 samples do not lead to the formation of new structural units (within the detection limit of the Raman technique),

and the Bi_2Se_3 is accommodative for impurity atoms. Furthermore, the binding energies of the pristine, as well as those of all the co-doped (BISS) samples, were obtained and shown in Figure 3. The survey scan for both the pristine and the co-doped samples are compared (Figure S2). The co-doping effect is evidently more pronounced for the highly doped sample (BISS-0.2), which shows the prominent impurity signal at binding energies of 452.68 eV. This binding energy corresponds to that of In.^{35,36} This implies that the Bi site's substitution does not show significant structural changes to the parent material.

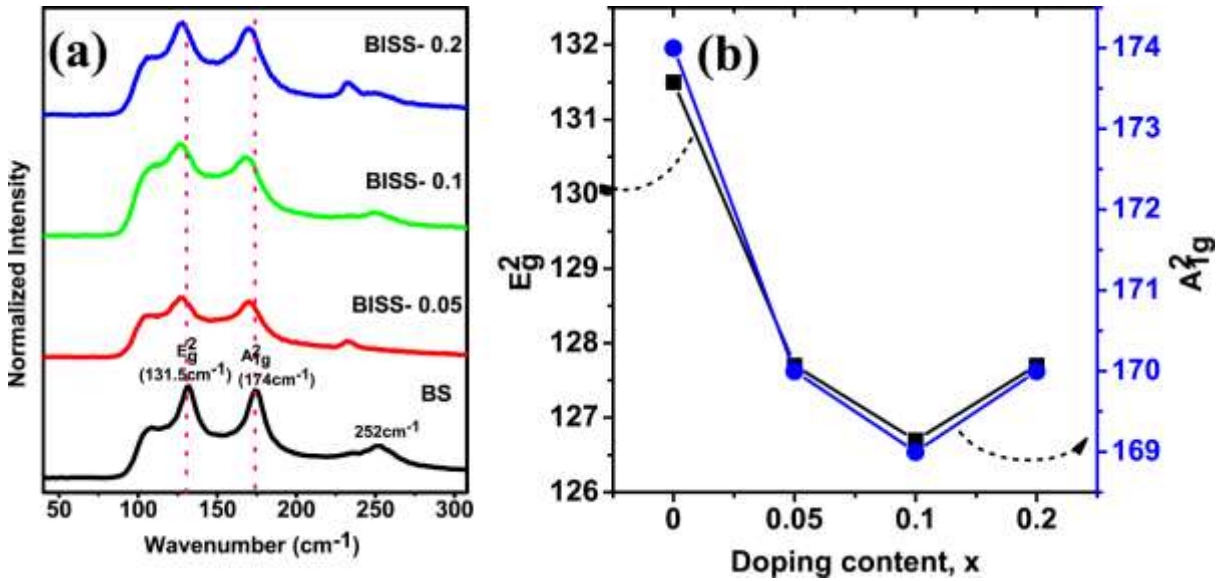


Figure 2. (a) Raman spectra (b) the individual Raman shift for all the synthesized BISS samples

Similarly, the high-resolution spectra for all the BS (Bi and Se) and BISS (Bi, In, Sb and Se) samples are depicted in Figure 3 and Table S3. Typically, the XPS spectra for the high-resolution data is fitted using the Gaussian function. The two prominent peaks, each at 158.09 eV and 163.23 eV for the pristine, can be ascribed to Bi $4f_{7/2}$ and Bi $4f_{5/2}$ (Figure 3a). It is observed that both the Bi $4f_{7/2}$ and Bi $4f_{5/2}$ shifted by an energy difference of 0.3 – 0.6 eV with an increase in In and Sb doping content. Thus, this demonstrates that in the absence of any new structural units in the doped samples, the band structure of the final $\text{Bi}_{2-x}\text{In}_x\text{Sb}_{2x/3}\text{Se}_3$ topological insulator is significantly influenced.³⁷ Again, the binding energy at 54.21 eV and 53.37 eV in Figure 3b are well assigned to Se $3d_{3/2}$ and $3d_{5/2}$. The Se $3d$ orbitals of the BISS samples remained unchanged after doping. From Figure 3c, the In $3d$ binding

energy located at 444.61 eV and 452.68 eV well matches that of In 3d_{5/2} and In 3d_{3/2}, respectively.^{36,38} As can be observed, two extra peaks located at 440.7 eV and 464.48 eV is shown in Figure 3c and Table S4. The peak at 440.7 eV represents In⁰ produced from the splitting of the 3d_{5/2}, while that at 464.48 eV represents the plasmon loss feature of the indium metal.³⁹ Figure 3d shows the presence of the Sb impurity in the final material. The binding energy of 529.77 eV and 539.35 eV (Table S4) is well assigned to the Sb 3d_{5/2} and Sb 3d_{3/2} of the BISS-0.05 samples.^{40,41} As the doping content is further increased (0.1 at.% and 0.2 at.%), this energy varied slightly (0.13 eV and 0.48 eV) correspondingly.

The rearrangement of the core energy levels in the valence band of the host by the impurity atoms contributes to the redistribution of all electrons in the host. Therefore, it changes the Fermi level (E_F) position and the density of conducting charge carriers around the E_F . The strategy is proven experimentally in the BISS compositions, whereby indium and antimony co-doping creates deep defect states of ~15 eV below the Fermi level. The defect states perturb the substantial electron population while leaving the impurity atoms with no net charge. Principally, this doping approach prevents the formation of ionized (which scatters conduction electrons) impurities in the semiconductor material.

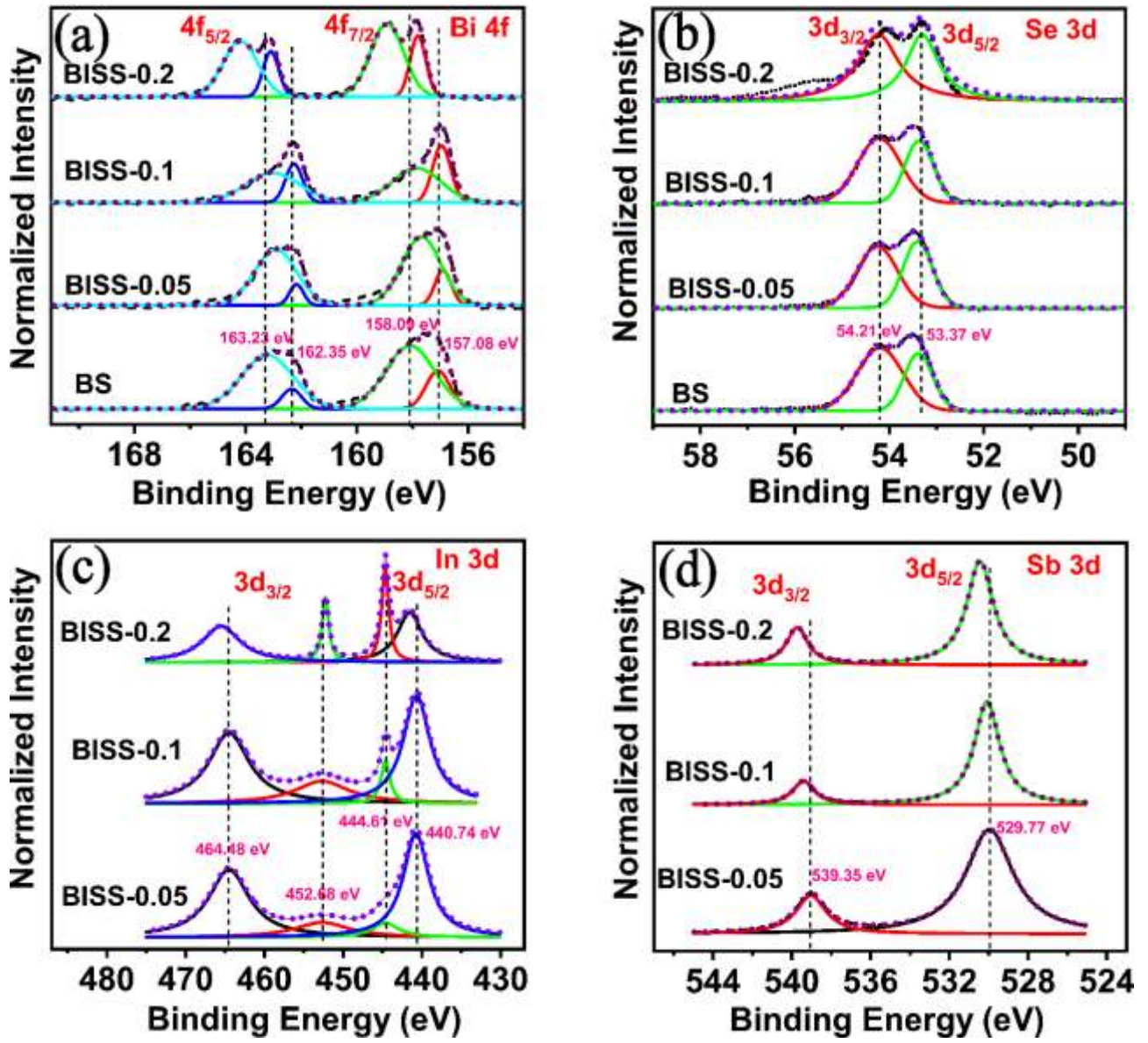


Figure 3. High-resolution XPS spectra of (a) Bi 4f (b) Se 3d (c) In 3d and (d) Sb 3d core-level of the BISS samples.

Table 1 Room temperature TE properties of BISS materials and the calculated m^*

Samples	n_{Hall} ($10^{19}cm^{-3}$)	μ_{Hall} ($cm^2V^{-1}s^{-1}$)	σ_{Hall} (Scm^{-1})	σ_{ZEM} (Scm^{-1})	S (μVK^{-1})	κ_T ($Wm^{-1}K^{-1}$)	$m^*(m_e)$
BS	0.186	149	44.342	36.17	-109.402	0.757	0.082
BISS-0.05	9.168	7.127	102.73	143.77	-94.89	0.502	0.639
BISS-0.1	7.382	3.351	91.96	95.28	-117.33	0.412	0.733
BISS-0.2	1.129	2.357	33.02	23.46	-137.98	0.246	0.329

In Table 1, we have shown the variation of the electron density with In and Sb co-doping in the Bi_2Se_3 structure. The electron density increases with mild doping ($x = 0.05$ at.%), which then decreases afterwards as the doping amount is further increased ($x > 0.05$ at.%). From the DFT calculation, the Fermi energy shift towards the conduction band with the co-doping. This is expected to enhance the electron density. However, on the contrary, the electron density initially increases and then decreases afterwards. This is because the substitution of In for Bi does not yield more electrons due to the available transition of $\text{In}(5s^25p^1)$ to form $\text{In}_{\text{Bi}}^x(5s^05p^3)$. Thus, the variation of the electron density is caused by the intrinsic contribution from point defects.⁴² The incorporation of In at the Bi site inhibit the volatilization of the selenium during the annealing process, which thus decreases the selenium vacancies. This, therefore, decreases the electron density, as shown in Table 1. With regards to this mechanism, similar work is reported elsewhere.^{43,44}

More so, field-emission gun scanning electron microscopy (FEG-SEM) is used to characterize the morphology and crystallite size of the samples. As shown in Figure S3a-d, a plate-like morphology is found for all the samples. The average crystallite size reduction observed by XRD is also in good agreement with the observed grain size indicated by SEM (linear intersecting method). It is worth noting that, as the doping amount increases from 0 at.% to 0.2 at.%, the crystallite size decreases, which corresponds well with that estimated from the Scherrer approach. The decrease in the crystallite size with co-doping comes from the pinning effect induced by the In and Sb doping⁴⁵ during the thermal treatment process.⁴⁶ This enhances the crystal boundaries and therefore reduces the thermal conductivity. Similarly, Energy dispersive x-ray (EDX) measurement was performed to estimate the exact atomic fractions of individual constituents of the BISS samples (Figure S4a-d). It is evident from the EDX spectra shown in Figure S4 that the doping process was successful.

Using DFT, we have theoretically studied the In and Sb co-doping effect on the Bi_2Se_3 topological insulator. The results are shown in Figures 4 and 5. Ideally, introducing an impurity atom into a host matrix (aliovalent doping) increases the charge density of the final material. However, the behaviour of the electronic configuration of Bi ($[\text{Xe}] 4f^{14} 5d^{10} 6s^2 6p^3$) and In ($[\text{Kr}] 4d^{10} 5s^2 5p^1$) and the

difference in the electronegativity ($\chi_{\text{Bi}} \sim 2.69$ and $\chi_{\text{In}} \sim 2.29$)⁴⁷ may result in more ionic bonding with strong carrier scattering and thus higher effective mass along with lower mobility of the charge carriers (see Table 1). Isovalent doping, unlike aliovalent doping, introduces neutral charge impurities into the crystal lattice of the parent material, and these neutral impurities oppose less to conduction electrons. However, a complex structure, irrespective of the doping approach, introduces more disorder in the material, which can scatter phonon and conduction electrons, i.e. diffusive transport can be the consequence. Similarly, a signature of effective phonon scattering, which causes a significant reduction in lattice conductivity, also deteriorates carrier mobility. Thus, the vast decrease in mobility observed for the BISS samples signifies the enhanced electron-phonon scattering, which decreases the mean free path of conduction electrons.⁴⁸

Herein, we show that the deep defect states (~ 15 eV below the Fermi level) and Fermi energy shift towards the conduction band (Figure 4a-d) are instigated by the In and Sb co-doping, resulting in enhanced electronic properties (Figure 5a-d).

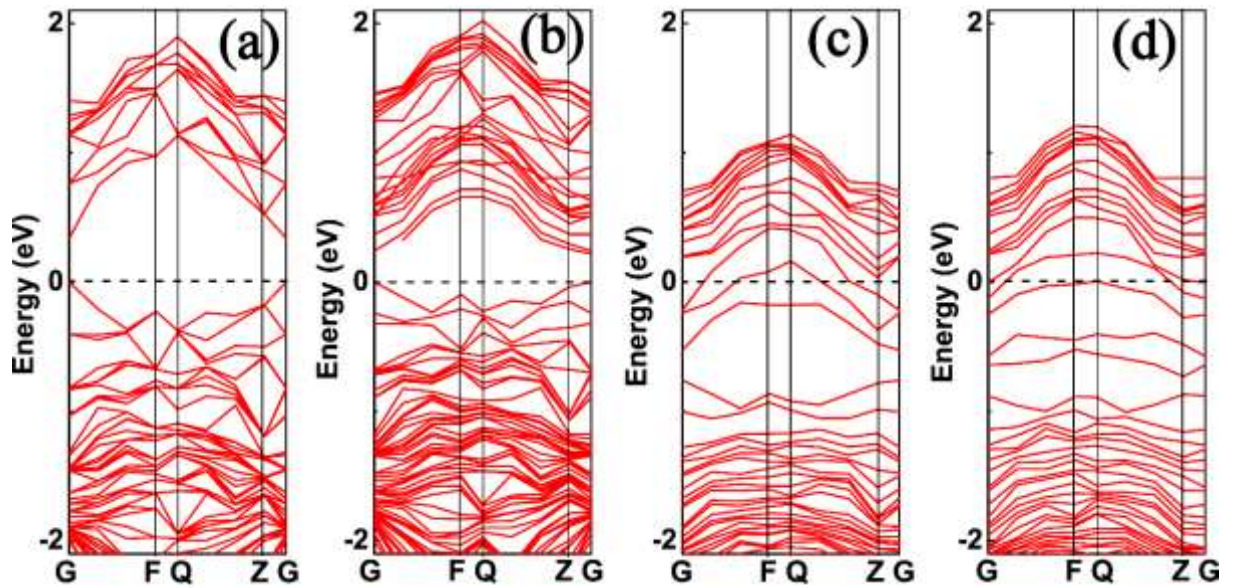


Figure 4. The Band structure for (a) BS (b) BISS-0.05 (c) BISS -0.1 (d) BISS-0.2 obtained from the DFT calculation

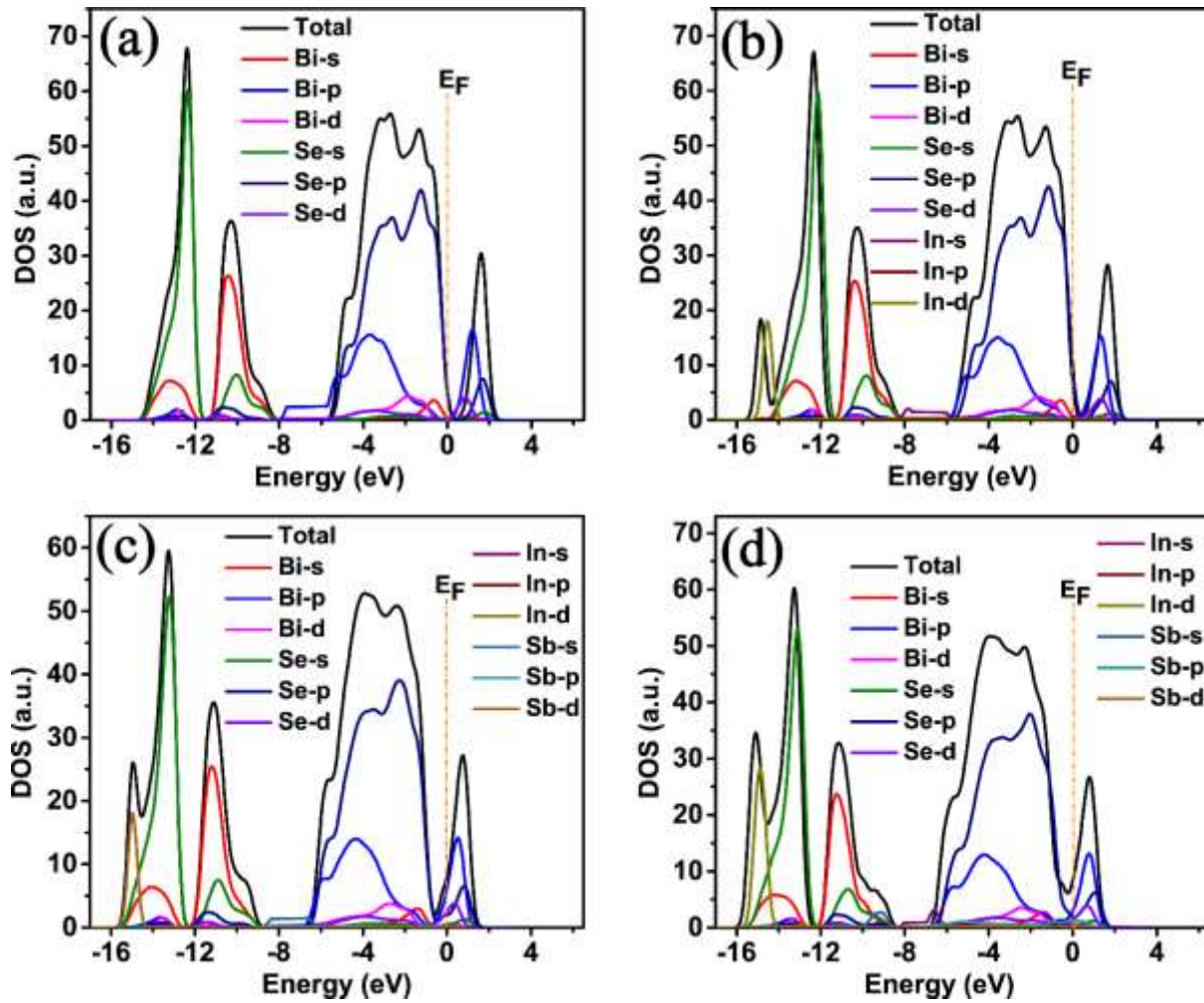


Figure 5. The DFT calculation of the PDOS of (a) pristine (b) BISS-0.05 (c) BISS-0.1 (d) BISS-0.2

The substitutional impurity (In) is responsible for the emerged defects states located below the Fermi level. In this system, no charge transfer from the impurity to the host is favoured; however, restructuring the electronic band induced by the impurity atom leads to improvement in the DOS due to the changes in the Fermi energy.

Certain impurity atoms have been shown to establish a pair of defects states in semiconductor materials, namely, the hyper deep defect states (HDS), which are inactive states located far below the Fermi energy and deep defect states (DDS), near the energy gap.^{49,50} In most cases, the DDS forms the resonant states as it hybridizes with the conduction band leading to excessive improvement in the DOS for the host material. It is clear that only HDS is evident from our DFT calculation; however, the shift of the Fermi level towards the conduction band is pronounced and contributed to the enhancement of the transport properties of our doped samples.

The electrical conductivity (σ_{ZEM}), as well as the Seebeck coefficient of all our samples, were simultaneously measured from 300K to 473 K using the procedure described in our previous work.³⁰ The electrical conductivity (Figure 6a) increases linearly with temperature throughout the entire temperature range for all the samples. The room temperature σ increases sharply with doping from the pristine (36 Scm⁻¹) to $x = 0.05$ at.% (144 Scm⁻¹). With a further increase in doping, the electrical conductivity deteriorated appreciably for $x = 0.1$ at. % (95 Scm⁻¹) and $x = 0.2$ at.% (24 Scm⁻¹). The massive enhancement in the electrical conductivity for the least doped sample ($x = 0.05$ at. %) is associated with the enhanced carrier density ($\sigma_{ZEM} = ne\mu$). The improved n compensated for the loss in carrier mobility (Table 1). The carrier mobility (compared to the pristine) observed for all the BISS samples are severalfold lower than that already reported for the $\text{Bi}_{2-x}\text{In}_x\text{Sb}_{2x/3}\text{Te}_3$.²⁵ This is because Bi_2Se_3 topological insulators possess lesser Van der Waals gaps and volume than Bi_2Te_3 . This implies the latter can accommodate a higher concentration of impurities compared to that of the former. Moreover, the drastic decrease in the carrier mobility can be related to the electronegativity difference between In and Bi, leading to more ionic bonding and thus, promoting higher DOS with lower mobility. It is worth mentioning that the choice of the isovalent doping approach is to reduce ionised impurities scattering in the host crystal that averts excessive carrier scattering. However, the measured carrier mobility reduction obtained for all the doped samples signifies significant lattice distortion induced scattering⁵¹ and electron-phonon scattering,⁵² thus deteriorating the mean free path of conduction electrons.⁴⁸ UV-Vis spectroscopy analysis was also carried out, and the results are provided in Figure S5. It can be seen that the optical density of the synthesized samples increases with doping, with the maximum density situated within 1.2 – 1.6 eV. The increase in density with doping (Figure S5) is in good agreement with the DFT calculation (Figure 5a-d). Despite the rise in Fermi energy with doping (Figures 4 and 5), there is a noticeable decrease in the carrier concentration for the samples BISS-0.1 and BISS-0.2. The reduction in the carrier concentration can be attributed to the filtering of the low energy charge carriers.^{53,54} Nanostructures can enhance the material power factor via the energy filtering effect. In this case, the charge carriers with low kinetic energies are impeded by potential from a nanoprecipitate phase, while high energy carriers experience no

restriction. This decreases the carrier concentration and, therefore, suggests that an optimal thermoelectric efficiency exists for an intermediate doping level. The consequence of energy filtering is that a mechanism of enhancement in the Seebeck coefficient through the energy-dependent scattering mechanism is strengthened, leading to carrier localization and hence a decrease in the actual carrier concentration. The high Seebeck coefficient and low thermal conductivity of the BISS-0.1 sample compensated for the slight drop in carrier concentration leading to optimal thermoelectric performance in all the synthesized samples. Considering our experimental and theoretical calculation together, the effective mass and Fermi energy of all the synthesized samples are independent of carrier concentration.

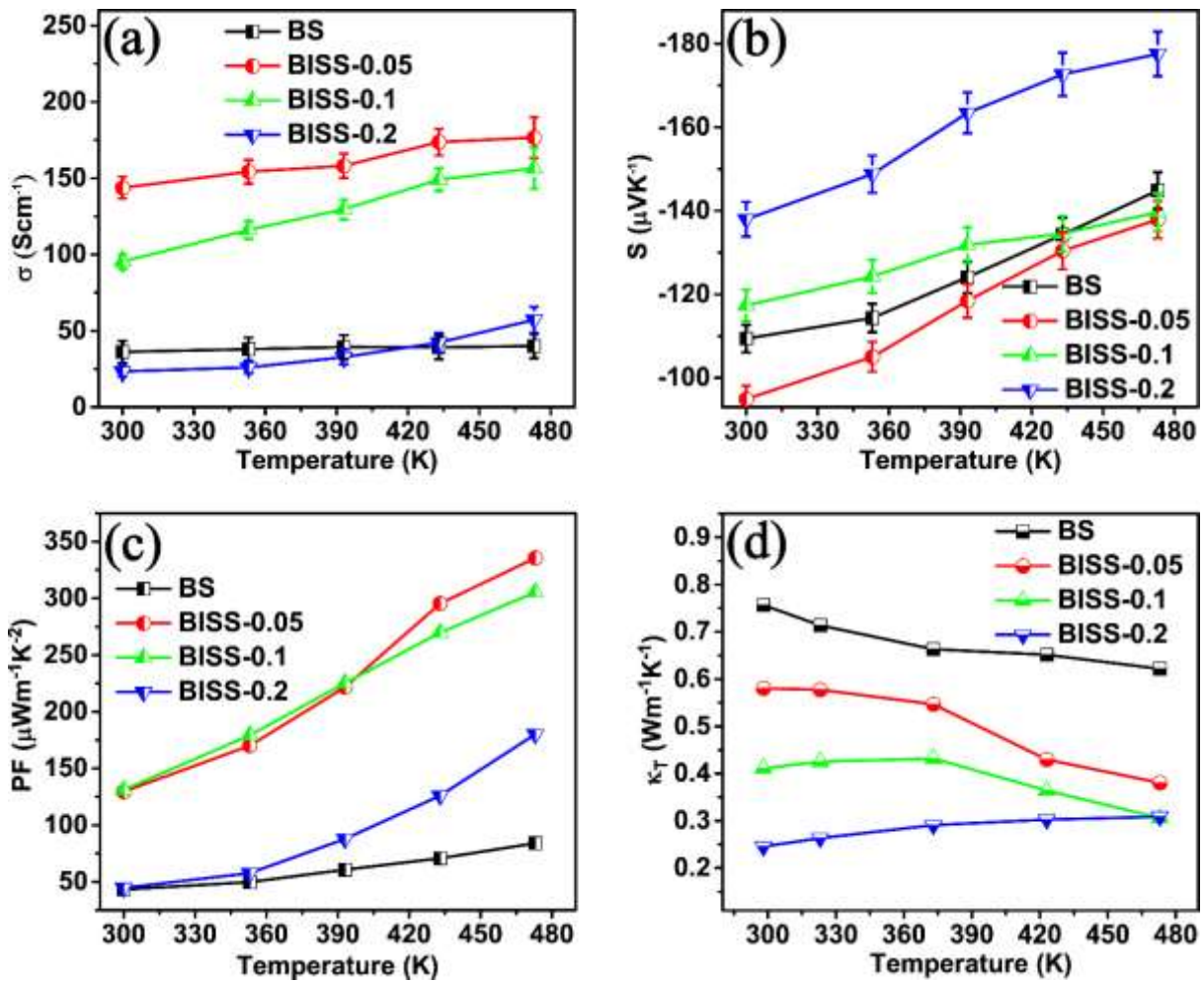


Figure 6. Temperature dependence of the (a) electrical conductivity (b) Seebeck coefficient (c) calculated power factor (d) the total thermal conductivity of the BISS samples

The Seebeck coefficient (Figure 6b) for all the BISS samples shows negative values from 300 K to 473 K representing a typical n-type behaviour. The Seebeck coefficient is sensitive to the asymmetry of the electronic density of state (DOS) near the Fermi level (E_F). This implies that infinitesimal changes in the DOS would affect the carrier density (n) and hence the magnitude of S . The carrier density of the BS and BISS samples are quantified by the Hall measurement, where all the BISS ($n \sim 10^{19}$) samples were approximately ten-fold higher than that of the pristine ($n \sim 10^{18} \text{ cm}^{-3}$). Using the linear dependence of S ; the effective mass is estimated using the semi-classical Mott-Jones formula,^{55,56} viz

$$\frac{S}{T} = -\frac{\pi^2 K_B^2}{3|e|} \left. \frac{\partial \ln \sigma(E)}{\partial E} \right|_{E_F} = -\frac{\pi^2 K_B^2}{(3\pi^2)^{2/3} \hbar^2 |e|} \frac{m^*}{n^{2/3}} \quad (1)$$

where κ_B , n , e , T , E_F , m^* , \hbar and σ are Boltzmann constant, carrier density, electrical charge, temperature, Fermi energy, effective mass, Plank's constant and electrical conductivity, respectively. From Eqn 1, the carrier effective mass is estimated. The obtained effective mass increases from the pristine (0.08 m_e) to $x = 0.1$ at. % (0.73 m_e). Upon further doping ($x = 0.2$ at. %), the effective mass decreases appreciably to 0.3 m_e . The improvement seen in the Seebeck coefficient for the BISS samples is ascribed to an improved modification of the DOS and effective tuning of n caused by the co-doping.

Figure 6c represents the calculated power factor for all the synthesized BISS ($0 \leq x \leq 0.2$) samples. The simultaneous improvement of σ and S is evident in the calculated PF . All the BISS samples showed better performance than that of the undoped samples considered between 300K and 473 K. The maximum PF ($0.337 \times 10^{-3} \text{ Wm}^{-1}\text{K}^{-2}$ at 473 K) in our studied samples was found for BISS-0.05. Compared with Bi_2Te_3 ,²⁵ Bi_2Se_3 in this work showed a better response of In and Sb co-doping. The observed simultaneous improvement in S , σ and hence PF is crucial for realizing high overall thermoelectric efficiency.

Utilizing nanostructured materials for thermoelectric energy generation is crucial for obtaining reduced total thermal conductivity, K_T . The reduction of thermal conductivity in crystalline materials below the amorphous limit is problematic. However, exploiting nanostructured materials plays a

significant role in enhancing K_T reduction, which influences the enhancement of the thermoelectric figure of merit. Here, the temperature dependence of the overall total thermal conductivity of the pristine and the BISS samples are estimated and shown in Figure 6d. The K_T of the BISS-0.05 follows a similar decreasing pattern throughout the entire temperature range as that of the pristine. However, as the doping amount reaches $x = 0.1$ at.%, the thermal conductivity slightly increases from 300 K to 375 K but decreases sharply afterwards. For the highly doped sample ($x = 0.2$ at. %), K_T increases from 300 K to 473 K. The calculation of the total thermal conductivity was done using the measured thermal diffusivity (Figure S6a), specific heat capacity (Figure S6b) and the density of the sample.³⁰ The electronic contribution (Figure S6c) to the total thermal conductivity (K_{el}) is calculated from the Wiedemann – Franz relation, $K_{el} = \sigma LT$, where L is the Lorentz factor which is calculated using Eqn S7, σ is the measured electrical conductivity, and T is the temperature. Using the obtained K_{el} data, the lattice thermal conductivity (shown in Figure S6d) is calculated from $K_{lat} = K_T - K_{el}$. The K_{lat} values for all the samples follow the same K_T trend with the minimum value of $0.25 \text{ Wm}^{-1} \text{ K}^{-1}$ at 300 K found for BISS-02. Therefore, the K_{lat} and the K_T values for all the BISS samples are lower than that of the pristine. This is due to the enhanced scattering of phonon energy caused by the synergistic effect of the small crystallite size, microstrain and lattice distortion instigated by the co-doping.

The lattice thermal conductivity of the BISS significantly decreases with increasing doping content from $x = 0$ to $x = 0.2$ at.%. For instance, the K_{lat} values of the $x = 0, 0.05$, and 0.1 at.% samples at 473 K are $0.62, 0.38$ and $0.30 \text{ Wm}^{-1} \text{ K}^{-1}$, respectively, as shown in Figure S6(d). When increasing the doping content from $x = 0.1$ at.% to $x = 0.2$ at.%, K_{lat} remains unchanged. The enhanced reduction in K_{lat} is ascribed to the following reasons. (1) The crystallite size and the bulk density (6.71 gcm^{-3}) gradually decrease with increasing doping content, as discussed in Figure S1. The small crystallite size provides a large area of crystal boundaries, which contributes to phonon scattering, acting as centers for long-wavelength phonon scattering;¹⁰ (2) the large differences in atomic mass ($\text{Bi} \rightarrow 208.98$, $\text{In} \rightarrow 114.82$, and $\text{Sb} \rightarrow 121.76 \text{ g mol}^{-1}$) and ionic radius ($\text{Bi}^{3+} \rightarrow 1.03$, $\text{In}^{3+} \rightarrow 0.8 \text{ \AA}$, $\text{Sb}^{3+} \rightarrow 0.76 \text{ \AA}$) between the host atom (Bi) and the doped atoms (In and Sb) give rise to the mass and strain field fluctuations in the crystal lattice, which enhance the short-wavelength phonon scattering

and a corresponding reduction in K_{lat} .^{57–59} It is worth to note that further doping in Bi_2Se_3 beyond $x = 0.1$ at.% is undesirable.

More importantly, the small crystallite size provides sufficient boundaries that promote grain boundary scattering and reduce lattice thermal conductivity. Although introducing impurities into a host material has served as an efficient mechanism to enhance thermal conductivity reduction, excessive doping can adversely affect K_T .⁶⁰ In that regard, upon realizing the sudden increasing trend of the K_{lat} and K_T in BISS-0.2 (Figure S7), it was sufficient not to proceed with further doping. As a result, we show an attainable minimum value of $0.25 \text{ Wm}^{-1}\text{K}^{-1}$ for BISS-0.2, which is much lower than the K_T previously reported.^{30,61} The low total thermal conductivity for all the BISS samples and the simultaneous enhancement of the Seebeck coefficient and electrical conductivity ensure higher TE efficiency. However, the small value of K_T for BISS-0.2 could not compensate for the low power factor, which affected the ZT. We have also provided the thermogravimetric data (Figure S8) for all the synthesized samples. The graph shows that the most stable samples are BISS-0.05 and BISS-0.1, while BISS-0.2 is the most unstable, especially at $T > 500 \text{ K}$.

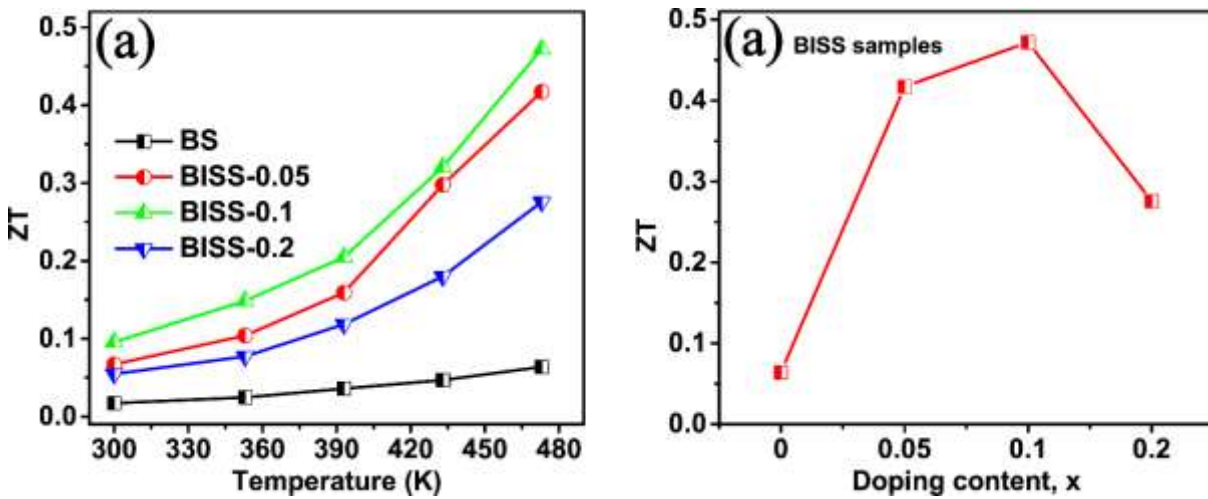


Figure 7. The thermoelectric figure of merit (ZT) (a) dependence on temperature for all the BISS samples (b) the maximum ZT dependence on doping content at 473K

The thermoelectric figure of merit, ZT dependence on temperature and doping amount for all the $\text{Bi}_{2-x}\text{In}_x\text{Sb}_{2x/3}\text{Se}_3$ samples are estimated and shown in Figure 7a and Figure 7b, respectively. The

dimensionless figure of merit increases with temperature for all the BISS samples. However, the impact of the doping amount is peaked at $x = 0.1$ at.%. This shows that the higher doping amount ($x = 0.2$ at.%) is detrimental to the enhancement of the ZT. The maximum ZT of 0.47 at 473K is found for BISS-0.1, representing 8 times enhancement compared to that of the pristine ($ZT = 0.06$) considered at the same temperature. It is evident from the measured electronic and thermal transport properties that the enhancement observed for BISS-0.1 is due to the optimized simultaneous enhancement of the Seebeck coefficient and electrical conductivity coupled with the reduced thermal conductivity. This implies isovalent doping plays a crucial role in enhancing thermoelectric performance. We have compared the superiority of our synthesized samples with those already reported (Table S5). Our design has erupted massive improvement in the TE properties.

Conclusions

In this work, $\text{Bi}_{2-x}\text{In}_x\text{Sb}_{2x/3}\text{Se}_3$ samples were synthesized through a single step thermal route. By introducing co-doping of In and Sb into the Bi_2Se_3 , simultaneous enhancement of the Seebeck coefficient and electrical conductivity was achieved, which led to improvement in the power factor. The simultaneous increase in S and σ for the Bi_2Se_3 topological insulator is possible by using isovalent dopants (In and Sb). The small crystallite size coupled with the lattice distortion caused by the slight difference in the ionic radii of the host and the impurities increases the pinning of the phonon vibration and hence decreases the total thermal conductivity. An optimum thermoelectric performance ($ZT_{\text{max}} = 0.47$ at 473 K) was found for BISS-0.1 material. To the best of our knowledge, the performance obtained from this work is higher than the existing Cu doped Bi_2Se_3 thermoelectric performance. Conventionally, introducing an impurity atom (aliovalent doping) for the host in a semiconductor in modern electronic technology creates either donor or acceptor levels showing that the band structure of the host materials remains unchanged after doping through rigid band approximation. This implies that the dopant transfers electrical charge to the host, thus promoting a change in the total number of free charge carriers in the semiconductor. This theory is valid when the

valence band of the impurity atom differs from that of the host. We show that adopting isovalent doping can simultaneously enhance the Seebeck coefficient and electrical conductivity with measurable deterioration in the thermal conductivity instigated by the In and Sb doping and defect states below the Fermi energy. Nonetheless, Bi ($6p^3$) substitution with In ($5s^25p^1$) is expected to restrict conduction electron scattering. However, the drastic decrease in the carrier mobility is due to the electronegativity difference between In and Bi, leading to more ionic bonding and thus, promoting higher DOS with lower mobility. The consequence of which is the enhancement power factor with a reduction in thermal conductivity. This is because effective doping has been successfully utilized to optimize the charge carrier density, thus promoting substantial improvement in the electronic properties and ZT.

Supporting Information

Lattice parameters and dislocation density calculated for all the samples, Energy dispersive spectra (EDX) of all the $\text{Bi}_{2-x}\text{In}_x\text{Sb}_{2x/3}\text{Se}_3$ samples, XPS data of all the samples, Comparison of pristine and doped Bi_2Se_3 thermoelectric materials, Crystallite size and microstrain, FESEM images, Thermal properties obtained for all the samples,

Acknowledgement

We wish to acknowledge grants from the Research Grants Council of Hong Kong Special Administrative Region Project no. T42-103/16N. Work at NUST "MISiS" was supported by the Ministry of Science and Higher Education of the Russian Federation in the framework of Increase Competitiveness Program of NUST "MISiS" (No. K2-2020-045) implemented by a governmental decree dated 16th of March 2013, N211.

References

- (1) Liu, W.D.; Wang, D. Z.; Liu, Q.; Zhou, W.; Shao, Z.; Chen, Z. G. High-Performance GeTe-Based Thermoelectrics: From Materials to Devices. *Adv. Energy Mater.* **2020**, *10* (19), 1–24.

<https://doi.org/10.1002/aenm.202000367>.

- (2) Pei, Y.; Wang, H.; Snyder, G. J. Band Engineering of Thermoelectric Materials. *Adv. Mater.* **2012**, *24* (46), 6125–6135. <https://doi.org/10.1002/adma.201202919>.
- (3) Wang, Y.; Liu, S.; Wu, Z.; Liu, G.; Yang, X.; Wei, T.; Wang, Q.; Ye, Y.; Li, D.; Zhu, J. Enhanced Thermoelectric Performance of Van Der Waals Tellurium via Vacancy Engineering. *Mater. Today Phys.* **2021**, *18*, 100379. <https://doi.org/10.1016/j.mtphys.2021.100379>.
- (4) Zheng, Z. H.; Shi, X. L.; Ao, D. W.; Liu, W. D.; Chen, Y. X.; Li, F.; Chen, S.; Tian, X. Q.; Li, X. R.; Duan, J. Y.; Ma, H. L.; Zhang, X. H.; Liang, G. X.; Fan, P.; Chen, Z. G. Rational Band Engineering and Structural Manipulations Inducing High Thermoelectric Performance in N-Type CoSb₃ Thin Films. *Nano Energy* **2021**, *81*, 105683. <https://doi.org/10.1016/j.nanoen.2020.105683>.
- (5) Hu, L.; Zhu, T.; Liu, X.; Zhao, X. Point Defect Engineering of High-Performance Bismuth-Telluride-Based Thermoelectric Materials. *Adv. Funct. Mater.* **2014**, *24* (33), 5211–5218. <https://doi.org/10.1002/adfm.201400474>.
- (6) Zhang, J.; Wu, D.; He, D.; Feng, D.; Yin, M.; Qin, X.; He, J. Extraordinary Thermoelectric Performance Realized in N-Type PbTe through Multiphase Nanostructure Engineering. *Adv. Mater.* **2017**, *29* (39), 1–7. <https://doi.org/10.1002/adma.201703148>.
- (7) Kulsi, C.; Kargupta, K.; Ganguly, S.; Banerjee, D. Enhanced Thermoelectric Performance of N-Type Bismuth Selenide Doped with Nickel. *Curr. Appl. Phys.* **2017**, *17* (12), 1609–1615. <https://doi.org/10.1016/j.cap.2017.09.004>.
- (8) Rejaul, S.; Shirolkar, M. M.; Dhara, B.; Kulkarni, S.; Deshpande, A. Enhancing the Thermopower and Tuning the Resistivity in Bi₂Se₃ with Fe-Doping. *Chem. Phys. Lett.* **2015**, *638*, 94–98. <https://doi.org/10.1016/j.cplett.2015.08.029>.
- (9) Devender; Gehring, P.; Gaul, A.; Hoyer, A.; Vaklinova, K.; Mehta, R. J.; Burghard, M.; Borca-

- Tasciuc, T.; Singh, D. J.; Kern, K.; Ramanath, G. Harnessing Topological Band Effects in Bismuth Telluride Selenide for Large Enhancements in Thermoelectric Properties through Isovalent Doping. *Adv. Mater.* **2016**, 6436–6441. <https://doi.org/10.1002/adma.201601256>.
- (10) Chen, Y. X.; Shi, X. L.; Zheng, Z. H.; Li, F.; Liu, W. Di; Chen, W. Y.; Li, X. R.; Liang, G. X.; Luo, J. T.; Fan, P.; Chen, Z. G. Two-Dimensional WSe₂/SnSe p-n Junctions Secure Ultrahigh Thermoelectric Performance in n-Type Pb/I Co-Doped Polycrystalline SnSe. *Mater. Today Phys.* **2021**, 16, 100306. <https://doi.org/10.1016/j.mtphys.2020.100306>.
- (11) Wang, Y.; Hong, M.; Liu, W. Di; Shi, X. L.; Xu, S. D.; Sun, Q.; Gao, H.; Lu, S.; Zou, J.; Chen, Z. G. Bi_{0.5}Sb_{1.5}Te₃/PEDOT: PSS-Based Flexible Thermoelectric Film and Device. *Chem. Eng. J.* **2020**, 397, 125360. <https://doi.org/10.1016/j.cej.2020.125360>.
- (12) Han, C.; Sun, Q.; Li, Z.; Dou, S. X. Thermoelectric Enhancement of Different Kinds of Metal Chalcogenides. **2016**, 6 (15), 1600498. <https://doi.org/10.1002/aenm.201600498>.
- (13) Yu, F.; Zhang, J.; Yu, D.; He, J.; Liu, Z.; Xu, B.; Tian, Y. Enhanced Thermoelectric Figure of Merit in Nanocrystalline Bi₂Te₃ Bulk. *J. Appl. Phys.* **2009**, 105 (9), 094303. <https://doi.org/10.1063/1.3120865>.
- (14) Baláž, P.; Baláž, M.; Achimovičová, M.; Bujňáková, Z.; Dutková, E. Chalcogenide Mechanochemistry in Materials Science: Insight into Synthesis and Applications (a Review). *J. Mater. Sci.* **2017**, 52 (20), 11851–11890. <https://doi.org/10.1007/s10853-017-1174-7>.
- (15) Siddique, A. R. M.; Mahmud, S.; Heyst, B. Van. A Review of the State of the Science on Wearable Thermoelectric Power Generators (TEGs) and Their Existing Challenges. *Renew. Sustain. Energy Rev.* **2017**, 73, 730–744. <https://doi.org/10.1016/j.rser.2017.01.177>.
- (16) Nielsch, K.; Bachmann, J.; Kimling, J.; Böttner, H. Thermoelectric Nanostructures: From Physical Model Systems towards Nanograined Composites. *Adv. Energy Mater.* **2011**, 1 (5), 713–731. <https://doi.org/10.1002/aenm.201100207>.
- (17) Li, Z.; Sun, Q.; Yao, X. D.; Zhu, Z. H.; Lu, G. Q. Semiconductor Nanowires for

- Thermoelectrics. *J. Mater. Chem.* **2012**, 22 (43), 22821–22831.
<https://doi.org/10.1039/c2jm33899h>.
- (18) Wei, J.; Yang, L.; Ma, Z.; Song, P.; Zhang, M.; Ma, J.; Yang, F.; Wang, X. Review of Current High-ZT Thermoelectric Materials. *J. Mater. Sci.* **2020**, 55 (27), 12642–12704.
<https://doi.org/10.1007/s10853-020-04949-0>.
- (19) Dargusch, M.; Liu, W. Di; Chen, Z. G. Thermoelectric Generators: Alternative Power Supply for Wearable Electrocardiographic Systems. *Adv. Sci.* **2020**, 7 (18), 1–13.
<https://doi.org/10.1002/advs.202001362>.
- (20) Liu, Y.; Wang, H.; Sherrell, P. C.; Liu, L.; Wang, Y.; Chen, J. Potentially Wearable Thermo-Electrochemical Cells for Body Heat Harvesting: From Mechanism, Materials, Strategies to Applications. *Adv. Sci.* **2021**, 8 (13), 1–23. <https://doi.org/10.1002/advs.202100669>.
- (21) Khan, S.; Kim, J.; Acharya, S.; Kim, W. Review on the Operation of Wearable Sensors through Body Heat Harvesting Based on Thermoelectric Devices. *Appl. Phys. Lett.* **2021**, 118 (20), 200501. <https://doi.org/10.1063/5.0049347>.
- (22) Zou, W. J.; Shen, K. Y.; Jung, S.; Kim, Y. B. Application of Thermoelectric Devices in Performance Optimization of a Domestic PEMFC-Based CHP System. *Energy* **2021**, 229, 120698. <https://doi.org/10.1016/j.energy.2021.120698>.
- (23) Mao, J.; Chen, G.; Ren, Z. Thermoelectric Cooling Materials. *Nat. Mater.* **2021**, 20 (4), 454–461. <https://doi.org/10.1038/s41563-020-00852-w>.
- (24) Sun, G.; Qin, X.; Li, D.; Zhang, J.; Ren, B.; Zou, T.; Xin, H.; Paschen, S. B.; Yan, X. Enhanced Thermoelectric Performance of N-Type Bi₂Se₃ Doped with Cu. *J. Alloys Compd.* **2015**, 639, 9–14. <https://doi.org/10.1016/j.jallcom.2015.03.124>.
- (25) Musah, J.; Guo, C.; Novitskii, A.; Serhienko, I.; Adesina, A. E.; Khovaylo, V.; Wu, C. L.; Zapien, J. A.; Roy, V. A. L. Ultralow Thermal Conductivity in Dual-Doped n-Type Bi₂Te₃ Material for Enhanced Thermoelectric Properties. **2021**, 2000910, 1–14.

<https://doi.org/10.1002/aelm.202000910>.

- (26) Guo, C.; Wei, S.; Zhou, S.; Zhang, T.; Wang, Z.; Ng, S.; Lu, X.; Wu, C. L.; Guo, W. Initial Reduction of CO₂ on Pd -, Ru -, and Cu-Doped CeO₂ (111) Surfaces: Effects of Surface Modification on Catalytic Activity and Selectivity. *ACS Appl. Mater. Interfaces* **2017**, 2 (111), 26107–26117. <https://doi.org/10.1021/acsami.7b07945>.
- (27) Nolan, M.; Grigoleit, S.; Sayle, D. C.; Parker, S. C.; Watson, G. W. Density Functional Theory Studies of the Structure and Electronic Structure of Pure and Defective Low Index Surfaces of Ceria. **2005**, 576, 217–229. <https://doi.org/10.1016/j.susc.2004.12.016>.
- (28) Wei, Z.; Xia, T.; Ma, J.; Feng, W.; Dai, J.; Wang, Q.; Yan, P. Investigation of the Lattice Expansion for Ni Nanoparticles. *Mater. Charact.* **2007**, 58 (10), 1019–1024. <https://doi.org/10.1016/j.matchar.2006.08.004>.
- (29) Arredondo, C. A.; Clavijo, J. I.; Aristizabal, A. J.; Gordillo, G. Investigation of AgInSe₂ Thin Films Grown by Co-Evaporation. *Conf. Rec. IEEE Photovolt. Spec. Conf.* **2009**, 886–891. <https://doi.org/10.1109/PVSC.2009.5411145>.
- (30) Musah, J.; Ilyas, A. M.; Novitskii, A.; Serhienko, I.; Egbo, K. O.; Saianand, G.; Khovaylo, V.; Kwo, S.; Man, K.; Roy, V. A. L. Effective Decoupling of Seebeck Coefficient and the Electrical Conductivity through Isovalent Substitution of Erbium in Bismuth Selenide Thermoelectric Material. *J. Alloys Compd.* **2020**, 857, 157559. <https://doi.org/10.1016/j.jallcom.2020.157559>.
- (31) Samoilov, A. M.; Buchnev, S. A.; Dolgoplova, E. A.; Yu. V. Synorov; Khoviv, A. M. Structural Perfection of PbTe Films Doped with Indium during Growth on Si Substrates. *Inorg. Mater.* **2004**, 40 (4), 349–354. <https://doi.org/10.1023/B:INMA.0000023953.49486.2a>.
- (32) Rajakarthy, R. K.; Muthukumaran, S. Investigation of Microstructure, Electrical and Photoluminescence Behaviour of Ni-Doped Zn_{0.96}Mn_{0.04}O Nanoparticles: Effect of Ni Concentration. *Opt. Mater. (Amst.)* **2017**, 69, 382–391.

<https://doi.org/10.1016/j.optmat.2017.05.007>.

- (33) Bindu, P.; Thomas, S. Estimation of Lattice Strain in ZnO Nanoparticles: X-Ray Peak Profile Analysis. *J. Theor. Appl. Phys.* **2014**, *8* (4), 123–134. <https://doi.org/10.1007/s40094-014-0141-9>.
- (34) Zhao, K.; Blichfeld, A. B.; Eikeland, E.; Qiu, P.; Ren, D.; Iversen, B. B.; Shi, X.; Chen, L. Extremely Low Thermal Conductivity and High Thermoelectric Performance in Liquid-like Cu₂Se_{1-x} S_x Polymorphic Materials. *J. Mater. Chem. A* **2017**, *5* (34), 18148–18156. <https://doi.org/10.1039/c7ta05788a>.
- (35) Jo, G.; Hong, W. K.; Maeng, J.; Kim, T. W.; Wang, G.; Yoon, A.; Kwon, S. S.; Song, S.; Lee, T. Structural and Electrical Characterization of Intrinsic N-Type In₂O₃ Nanowires. *Colloids Surfaces A Physicochem. Eng. Asp.* **2008**, *313*, 308–311. <https://doi.org/10.1016/j.colsurfa.2007.04.166>.
- (36) Khan, G. G.; Ghosh, S.; Sarkar, A.; Mandal, G.; Mukherjee, G. D.; Manju, U.; Banu, N.; Dev, B. N. Defect Engineered D₀ Ferromagnetism in Tin-Doped Indium Oxide Nanostructures and Nanocrystalline Thin-Films. *J. Appl. Phys.* **2015**, *118* (7). <https://doi.org/10.1063/1.4928952>.
- (37) Chen, B.; Li, J.; Wu, M.; Hu, L.; Liu, F.; Ao, W.; Li, Y.; Xie, H.; Zhang, C. Simultaneous Enhancement of the Thermoelectric and Mechanical Performance in One-Step Sintered n-Type Bi₂Te₃-Based Alloys via a Facile MgB₂ Doping Strategy. *ACS Appl. Mater. Interfaces* **2019**, *11* (49), 45746–45754. <https://doi.org/10.1021/acsami.9b16781>.
- (38) Zhang, S.; Zhang, J.; Liu, B.; Jia, X.; Wang, G.; Chang, H. Large Area Growth of Few-Layer In₂Te₃ Films by Chemical Vapor Deposition and Its Magnetoresistance Properties. *Sci. Rep.* **2019**, *9* (1), 1–7. <https://doi.org/10.1038/s41598-019-47520-x>.
- (39) Detweiler, Z. M.; Wulfsberg, S. M.; Frith, M. G.; Bocarsly, A. B.; Bernasek, S. L. The Oxidation and Surface Speciation of Indium and Indium Oxides Exposed to Atmospheric Oxidants. *Surf. Sci.* **2016**, *648*, 188–195. <https://doi.org/10.1016/j.susc.2015.10.026>.

- (40) Richter, W.; Kohler, H.; Becker, C. R. A Raman and Far-Infrared Investigation of Phonons in the Rhombohedral V₂-VI₃ Compounds. *Phys. Stat. Sol.* **1977**, *84*, 619.
- (41) Garje, S. S.; Eisler, D. J.; Ritch, J. S.; Afzaal, M.; O'Brien, P.; Chivers, T. A New Route to Antimony Telluride Nanoplates from a Single-Source Precursor. *J. Am. Chem. Soc.* **2006**, *128* (10), 3120–3121. <https://doi.org/10.1021/ja0582408>.
- (42) Li, F.; Zhai, R.; Wu, Y.; Xu, Z.; Zhao, X.; Zhu, T. Enhanced Thermoelectric Performance of N-Type Bismuth-Telluride- Based Alloys via In Alloying and Hot Deformation for Mid-Temperature Power Generation. *J. Mater.* **2018**, *4* (3), 208–214. <https://doi.org/10.1016/j.jmat.2018.05.008>.
- (43) Novotný, R.; Urbanová, E.; Horák, J. Optical Properties of Bi₂-XIn_xSe₃ Single Crystals. *Phys. status solidi A* **1989**, *615* (2), 615–622.
- (44) Novotný R; Losták P; Horák R. Bi₂-XIn_xSe₃ Crystals; Optical Properties and Transport Coefficients. *Phys. Scr.* **1990**, *42* (2), 253.
- (45) Park, K.; Seong, J. K.; Kim, G. H. NiO Added Zn_{1-x}Ni_xO (0 ≤ x ≤ 0.05) for Thermoelectric Power Generation. **2009**, *473*, 423–427. <https://doi.org/10.1016/j.jallcom.2008.05.101>.
- (46) Gao, L.; Zhai, S.; Liu, R.; Fu, N.; Wang, J.; Fu, G. Enhanced Thermoelectric Performance of CdO Ceramics Via Ba²⁺ Doping. **2015**, *3290*, 3285–3290. <https://doi.org/10.1111/jace.13780>.
- (47) Tantarini, Christian, O. R. A. Thermochemical Electronegativities of All Elements. *Nat. Commun.* **2021**, *12* (1), 1–9. <https://doi.org/10.1038/s41467-021-22429-0>.
- (48) Cho, H.; Kim, J. H.; Back, S. Y.; Ahn, K.; Rhyee, J. S.; Park, S. D. Enhancement of Thermoelectric Properties in CuI-Doped Bi₂Te_{2.7}Se_{0.3} by Hot-Deformation. *J. Alloys Compd.* **2018**, *731*, 531–536. <https://doi.org/10.1016/j.jallcom.2017.10.016>.
- (49) Hoang, K.; Mahanti, S. D. Electronic Structure of Ga-, In-, and Tl-Doped PbTe: A Supercell Study of the Impurity Bands. *Phys. Rev. B - Condens. Matter Mater. Phys.* **2008**, *78* (8), 1–8.

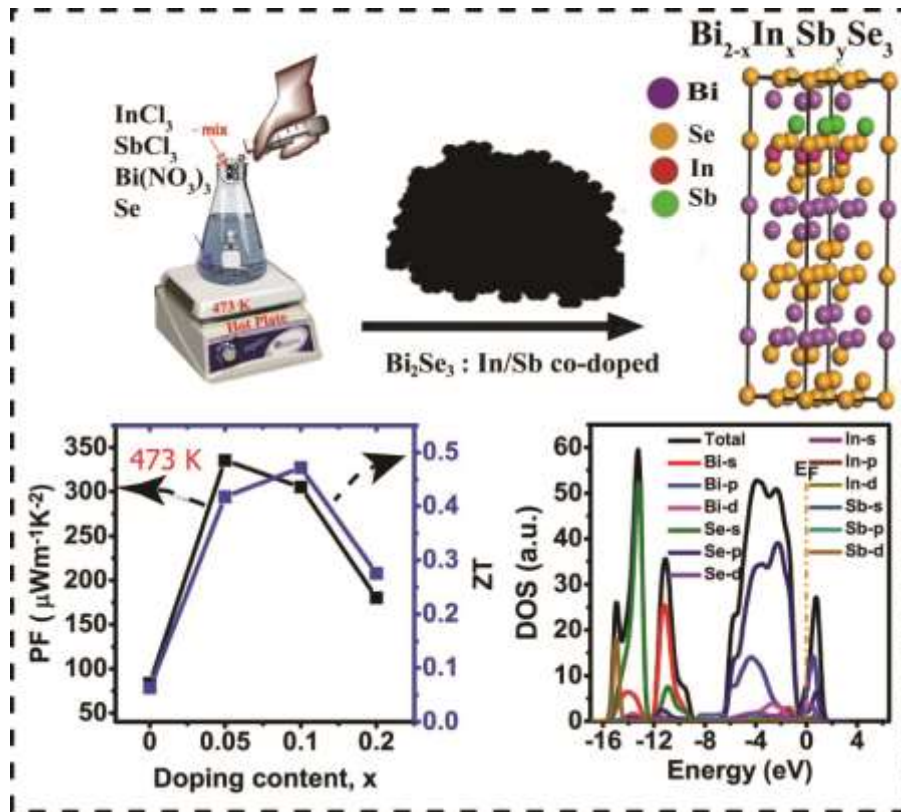
<https://doi.org/10.1103/PhysRevB.78.085111>.

- (50) Hjalmarson, H. P.; Vogl, P.; Wolford, D. J.; Dow, J. D. Theory of Substitutional Deep Traps in Covalent Semiconductors. *Phys. Rev. Lett.* **1980**, *44* (12), 810–813. <https://doi.org/10.1103/PhysRevLett.44.810>.
- (51) Zhu, T.; Xu, Z.; He, J.; Shen, J.; Zhu, S.; Hu, L.; Tritt, T. M.; Zhao, X. Hot Deformation Induced Bulk Nanostructuring of Unidirectionally Grown P-Type (Bi,Sb)₂Te₃ Thermoelectric Materials. *J. Mater. Chem. A* **2013**, *1* (38), 11589–11594. <https://doi.org/10.1039/c3ta12764h>.
- (52) Wang, S.; Tan, G.; Xie, W.; Zheng, G.; Li, H.; Yang, J.; Tang, X. Enhanced Thermoelectric Properties of Bi₂(Te_{1-x}Sex)₃-Based Compounds as n-Type Legs for Low-Temperature Power Generation. *J. Mater. Chem.* **2012**, *22* (39), 20943–20951. <https://doi.org/10.1039/c2jm34608g>.
- (53) Narducci, D.; Selezneva, E.; Cerofolini, G.; Frabboni, S.; Ottaviani, G. Impact of Energy Filtering and Carrier Localization on the Thermoelectric Properties of Granular Semiconductors. *J. Solid State Chem.* **2012**, *193*, 19–25. <https://doi.org/10.1016/j.jssc.2012.03.032>.
- (54) Kishimoto, K.; Tsukamoto, M.; Koyanagi, T. Temperature Dependence of the Seebeck Coefficient and the Potential Barrier Scattering of N-Type PbTe Films Prepared on Heated Glass Substrates by RF Sputtering. *J. Appl. Phys.* **2002**, *92* (9), 5331–5339. <https://doi.org/10.1063/1.1512964>.
- (55) Xiong, Q. Enhanced Thermoelectric Properties of Solution Grown Bi₂Te_{3-x}Sex Nanoplatelet Composites. *Nano Lett.* **2012**, *12* (3), 1203–1209.
- (56) Richter, J.; Friedrich, L.; Schiller, W. Temperature Dependence of the Thermoelectric Power of Disordered Alloys. **1982**, *151*, 151–160.
- (57) Abeles, B. Lattice Thermal Conductivity of Disordered Semiconductor Alloys at High

Temperatures. *Phys. Rev.* **1963**, *131* (5), 1906–1911.

<https://doi.org/10.1103/PhysRev.131.1906>.

- (58) He, J.; Kanatzidis, M. G.; Dravid, V. P. High Performance Bulk Thermoelectrics via a Panoramic Approach. *Mater. Today* **2013**, *16* (5), 166–176. <https://doi.org/10.1016/j.mattod.2013.05.004>.
- (59) Cha, J. S.; Kim, D. H.; Hong, H. Y.; Kim, G. H.; Park, K. Effect of La³⁺ Substitution on the Structural and Thermoelectric Properties of Ca_{3-x}La_xCo₄O_{9+δ}. *J. Eur. Ceram. Soc.* **2019**, *39* (11), 3320–3326. <https://doi.org/10.1016/j.jeurceramsoc.2019.04.030>.
- (60) Cao, R.; Zhu, Z.; Jian, X.; Xing, L.; Hongzhang, H. Enhanced Thermoelectric Properties of the Lu-Doped and CNT- Dispersed - Bi₂Te₃ Alloy. *Appl. Phys. A* **2019**, *125* (2), 126. <https://doi.org/10.1007/s00339-019-2427-x>.
- (61) Musah, J.-D.; Yanjun, X.; M. Ilyas, A.; G. Novak, T.; Jeon, S.; Arava, C.; V. Novikov, S.; S. Nikulin, D.; Xu, W.; Liu, L.; Md, A.; Lam, K.-H.; Chen, X.; Lawrence Wu, C.-M.; A. L. Roy, V. Simultaneous Enhancement of Thermopower and Electrical Conductivity through Isovalent Substitution of Cerium in Bismuth Selenide Thermoelectric Materials. *ACS Appl. Mater. & Interfaces* **2019**, *11* (47), 44026–44035. <https://doi.org/10.1021/acsami.9b11344>.



Synopsis

A novel doping strategy is implemented on Bi₂Se₃ material, leading to a high figure of merit for efficient waste energy recovery